Phase Field Benchmark Problems Targeting Fluid Flow and Electrochemistry

A. M. Jokisaari[a,b,*], W. Wu[a,b], P. W. Voorhees[a,c], J. E. Guyer[d], J. A. Warren[d], O. G. Heinonen[b,1]

[a] *Center for Hierarchical Materials Design, Northwestern University, 2205 Tech Drive, Suite 1160, Evanston, IL, 60208, USA*
[b] *Materials Science Division, Argonne National Laboratory, 9700 South Cass Avenue, Lemont, IL 60439, USA*
[c] *Department of Materials Science and Engineering, Northwestern University, 2220 Campus Drive, Evanston, IL 60208, USA*
[d] *Material Measurement Laboratory, National Institute of Standards and Technology, 100 Bureau Drive, MS 8300, Gaithersburg, MD 20899-8300*
[e] *Northwestern-Argonne Institute of Science and Engineering, 2205 Tech Drive, Suite 1160, Evanston, Illinois 60208, USA*

Abstract

In this work, we continue our development of phase field model benchmark problems with the addition of a third set, complimenting our previously developed problems for diffusion, precipitation, dendritic growth and linear elasticity. These benchmark problems are being jointly developed by the Center for Hierarchical Materials Design (CHiMaD) and the National Institute of Standards and Technology (NIST) along with input from the phase field community. The first problem in this third set targets Stokes flow, with a particular emphasis on flow around an obstruction placed asymmetrically in the domain. While Stokes flow is not traditionally in the canon of phase field problems, it is a class of problems gaining importance in areas such as filtration and water purification. The second problem deals with coupled Cahn-Hilliard diffusion and electrostatic forces, which is an important area in energy storage and battery sciences. We present our own solutions and discuss sources of numerical errors for the Stokes problem as well as simple checks to avoid fundamental issues in the coupled diffusion-electrostatics problem. The latter problem contains some subtleties that we expand on in an Appendix.

Keywords: phase field, benchmark, Stokes flow, electrochemistry

*Corresponding author, Present and permanent address: Computational Mechanics and Materials Department, Idaho National Laboratory, Idaho Falls, ID 83415

Email addresses: andrea.jokisaari@inl.gov (A. M. Jokisaari), wuw@anl.gov (W. Wu), p-voorhees@northwestern.edu (P. W. Voorhees), guyer@nist.gov (J. E. Guyer), james.warren@nist.gov (J. A. Warren), heinonen@anl.gov (O. G. Heinonen)

1. Introduction

For the past few years, the Center for Hierarchical Materials Design (CHiMaD) and the National Institute for Standards and Technology (NIST) have led an effort to develop benchmark problems for phase field modeling. The published problems have been developed with considerable community involvement and feedback, and we envisage that they will be useful and instructive as phase field modeling gains ground as an important component of Integrated Computational Materials Engineering (ICME). The problems are carefully constructed to stress aspects of numerical solutions of commonly-encountered coupled physics in phase field simulations. The benchmark problems are designed with two goals in particular: to test new algorithms or codes against results to ensure computational accuracy and to be used as a tool to train new researchers. The purpose of the benchmark problems publication series is to explain the rationale for choosing the problems and the aspects of numerical implementations that may be stressed in trying to solve the problems. We also include solutions that we have generated as examples, but the emphasis of the publications is on the construction of the problems and on useful metrics for comparison by practitioners. We deliberately choose to construct the benchmark problems from the canon of typical problems encountered in phase field modeling, and in particular with physics couplings that may be encountered frequently and which may pose challenges to computational modelers. Previous problem sets focused on the diffusion of solute and second phase coarsening [1], solidification of an undercooled liquid (dendritic growth) [2], and linear elasticity [2]. All of these problems are cast in terms of Cahn-Hilliard or Allen-Cahn equations with different free energy functionals, and they are true phase field problems in the sense that they contain phase field variables that vary smoothly across interfaces or phase boundaries.

In the third set of benchmark problems presented here, we explore two additional topics. The first problem in this set is of a Stokes fluid, which is not a true phase field problem but which is important in the description of fluids, solutions, and colloidal suspensions at the nano- or micrometer scale. Because fluid flow is included within the collections of models for mesoscale phenomena (see for example Refs. [3, 4]), we decided to include it in the set of benchmark problems. It also became evident during community discussions that the Stokes fluid problem is challenging for several traditional phase field computational modeling frameworks.

The second problem in this new set couples the Cahn-Hilliard equation with Poisson's equation for electrostatics. This coupling underlies basically all mesoscale modeling of electrochemical phenomena [5, 6], because they include diffusion of charged species (two examples of this are seen in Refs. [7, 8]). Thus, this benchmark problem can be thought of as a very simplified version of a fundamental problem in electrochemistry targeting a key coupling, even though for simplicity many aspects of a real electrochemistry problem have been removed. The problem also includes a curved surface, because curved geometries are likely to appear in electrochemical problems.

In this work, we will provide background and justification for the mathematical formulation of these problems. We will also present suggested metrics for how to evaluate solutions for the Stokes problem, and we will present and discuss example solutions that we have generated. The benchmark problems are also posted on our website (https://pages.nist.gov/pfhub/) and we encourage all readers to explore the additional resources there. This website serves

as a community resource with a repository for the problem statements and results posted by different groups, discussions around the benchmark problems, and other related information.

2. Model formulations

2.1. Stokes flow benchmark problem

The most general continuum formulation for fluid flow is the Navier-Stokes equation, which describes the conservation of momentum of a viscous, compressible fluid subject to external forces. The Navier-Stokes momentum equation is

$$\frac{\partial}{\partial t}(\rho \mathbf{u}) + \nabla \cdot (\rho \mathbf{u} \otimes \mathbf{u}) = -\nabla \cdot (p\mathbf{I}) + \nabla \cdot \boldsymbol{\tau} + \rho \mathbf{g}, \tag{1}$$

where ρ is the local fluid density, $\mathbf{u}$ the local fluid velocity field, $\otimes$ indicates the outer (tensor) product, p is the local pressure, $\mathbf{I}$ is the identity tensor, $\boldsymbol{\tau}$ is the deviatoric stress tensor arising from viscosity, and $\mathbf{g}$ is a field of external acceleration, arising from, e.g., gravity or electrostatic forces. The full Navier-Stokes equation is very difficult to solve. In particular, the term $\nabla \cdot (\rho \mathbf{u} \otimes \mathbf{u})$ describes inertial forces that give rise to turbulence.

The Stokes flow equations are special case of the full Navier-Stokes equations that are derived by applying several assumptions. Stokes flow equations apply to the steady flow of incompressible fluids at low Reynolds number. The Reynolds number is a measure of inertial forces relative to viscous forces in fluid flow; thus, low Reynolds numbers indicate that inertial forces can be ignored. Inertial forces are responsible for turbulence in flow. Physically, Stokes flow, also called creeping flow, occurs when fluid viscosity is high and fluid velocity is low, such that the fluid flow is laminar. As a result, the Stokes equation is well-suited to describe laminar flow in fluids.

A first simplification is to assume that the fluid is incompressible, which is a very reasonable approximation for studies that are concerned only with flow and not phenomena such as sound waves or shock waves in fluids. For incompressible fluids, the fluid is assumed to be isotropic, such that the deviatoric stress tensor can be expressed in terms of the dynamic viscosity μ,

$$\boldsymbol{\tau} = 2\mu \boldsymbol{\epsilon}, \tag{2}$$

where $\boldsymbol{\epsilon} = \frac{1}{2}\left(\nabla \mathbf{u} + (\nabla \mathbf{u})^{\mathrm{T}}\right)$ is the rate-of-strain tensor. In general, μ depends on local pressure and velocity. Therefore,

$$\boldsymbol{\tau} = \mu\left(\nabla \mathbf{u} + (\nabla \mathbf{u})^{\mathrm{T}}\right), \tag{3}$$

so

$$\nabla \cdot \boldsymbol{\tau} = \mu \nabla^2 \mathbf{u} \tag{4}$$

because $\nabla \cdot \mathbf{u} = 0$ for an incompressible fluid. Furthermore, by linearizing Eq. 1, the term in $\mathbf{u} \otimes \mathbf{u}$ is removed. Physically, this eliminates convective terms. Upon linearizing and using the assumption of incompressibility so that the density $\rho = \rho_0$ is constant, the equation

$$\rho_0 \frac{\partial \mathbf{u}}{\partial t} - \mu \nabla^2 \mathbf{u} + \nabla p - \rho_0 \mathbf{g} = 0 \tag{5}$$

results. Finally, steady flow is assumed, so that $\partial \mathbf{u}/\partial t = 0$, and the momentum equation for incompressible flow is given as

$$-\mu \nabla^2 \mathbf{u} + \nabla p - \rho_0 \mathbf{g} = 0. \tag{6}$$

In combination with Eq. 1, a fluid must obey a mass continuity equation, which in differential form is given as

$$\frac{\partial \rho}{\partial t} = \nabla \cdot (\rho \mathbf{u}) \,. \tag{7}$$

The continuity equation states that any increase or decrease in fluid mass in a volume element occurs because of the flow of mass into or out of the volume element. If the fluid is incompressible, the mass density ρ is constant in space and time, and the continuity equation becomes

$$\nabla \cdot \mathbf{u} = 0. \tag{8}$$

The combination of Eq. 6 and Eq. 8 give the *Stokes equation*. To solve for Stokes flow, suitable boundary conditions have to be supplied. These are usually related to how the fluid "sticks" to or "slips" at bounding surfaces, expressed as Dirichlet boundary conditions on the fluid velocity components.

When deriving the equations to be implemented for the numerical solution, care must be taken to specify the outlet boundary condition correctly. In general, Navier-Stokes problems may be solved in a pressure-based formulation if the formulation is for an incompressible fluid, or in a density-based formulation if the formulation is for a compressible fluid. In this work, the Stokes problem specified by Eqs. 6 and 8 assumes an incompressible fluid, and thus we solve the problem in a pressure-based formulation. Pressure enters the equations only via the gradient, and the weak forms of the equations (necessary, e.g., for finite element solution implementations) do not contain a boundary term for the pressure. Thus, we must specify the value of the pressure at one point to provide an actual value from which the rest of the pressure field may be calculated.

The Stokes benchmark problem has two parts, (a) and (b). Both parts consider flow in a two-dimensional (2D) channel and both parts are defined by the combination of Eq. 6 and Eq. 8. In part (a), the flow is unobstructed, while in part (b), the flow is obstructed with an elliptical obstruction. First, we fully specify part (a), which is also common to part (b).

The 2D channel computational domain for part (a) and part (b) consists of a rectangle 30 units long and 6 units wide (Fig. 1). Both part (a) and part (b) apply no-slip boundary conditions $u_x = u_y = 0$ on the upper ($y = 6$) and lower ($y = 0$) channel surfaces. At the left inlet ($x = 0$), the flow velocity is given by a parabolic profile

$$u_x(0, y) = -0.001(y - 3)^2 + 0.009, \;\; u_y(0, y) = 0. \tag{9}$$

Because the pressure only enters through its gradient, it is fixed by setting the pressure $p(30, 6) = 0$. In addition, the parameters $\rho_0 = 100$, $\mu = 1$, and $\mathbf{g} = (0, -0.001)$ are defined.

Part (b) is an extension of part (a). In part (b), the 2D channel computational domain also contains an elliptical obstruction within the channel. The obstruction is centered at $(7, 2.5)$ with a semi-major axis (along the y-direction) of $a = 1.5$, and a semi-minor axis (along the x-direction) of $b = 1$. No-slip boundary conditions ($u_x = u_y = 0$) are also applied on the surface of the obstruction.

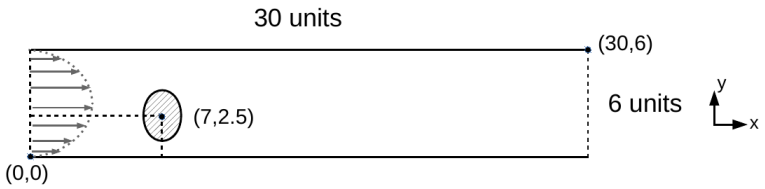

Figure 1: Schematic illustration of the 2D computational domain and inlet boundary condition (indicated by arrows) for the Stokes flow benchmark problem. In part (a) the domain is just the rectangle; in part (b) the domain has an additional elliptical obstruction in the channel.

Benchmark problems specify simple outputs as metrics for direct comparison of results. This problem is a steady-state problem and thus the outputs are fairly simple. In this problem, we will plot pressure and all components of the velocity field along the lines $y = 5$ and $x = 7$.

2.2. Coupled Cahn-Hilliard-Poisson benchmark problem

Charging or discharging batteries, electrodeposition, and electromigration are all examples of electrochemical problems. These problems typically involve the diffusion of charged species, such as ions or molecules, under the influence of forces, including long-range electrostatic forces arising from the charge distributions. The distribution of the charged species can be described with a concentration fields. A phase field formulation of an electrochemical problem requires a free energy, which includes chemical, electrostatic, and mechanical components (e.g., due to work done by applied pressure) as well as interfacial energies in terms of one or more phase fields [5]. The spatiotemporal evolution of the concentration fields typically includes sources and sinks arising from chemical reactions in addition to conserved currents; chemical reactions may also release or absorb energy. Models capturing all of these phenomena become complex.

Following the benchmark formulation ethos, we eschew the development of a realistic electrochemical problem capturing all of these phenomena and instead formulate a very simplified problem that only describes diffusion of a conserved species under the influence of concentration gradients and electrostatic forces. To maintain charge neutrality in the system, which is a reasonable physical constraint, a constant background charge density is added with a total charge equal in magnitude but opposite in sign to the total charge of the diffusing species described by the concentration field. In addition, we assume that the mobility of the concentration field, M, is concentration-dependent. This is not unreasonable because in many systems, such as colloidal or polymeric systems, increased species concentration "crowds" the system, making diffusion more difficult. A concentration-dependent mobility also distinguishes our model system from a well-known model of block-copolymer systems [9].

The benchmark problem involves a concentration field, c, of a charged species and the electrostatic potential field, Φ, that arises from the charged species as well as from an externally applied potential. We assume that the charge density, ρ, due to the diffusing concentration field is directly proportional to the concentration field. In addition to the mobile

concentration field c, we add a static background concentration field, c_0, such that the total charge in the system due to c and c_0 is zero. Thus, $\rho = q(c - c_0)$, where q is a constant unit of charge. For simplicity, the free energy of the concentration field is described using the same form as that in the spinodal decomposition benchmark problem [1] with the addition of the electrostatic free energy. The total free energy of the system is given as

$$F = \int_V \left[\frac{\kappa}{2} |\nabla c|^2 + f_{\text{chem}}(c) + f_{\text{elec}}(c, \Phi) \right] dV, \tag{10}$$

where κ is the gradient energy coefficient, f_{chem} is the chemical free energy density, and f_{elec} is the electrostatic free energy density. The f_{elec} term couples the charged concentration field c with the electrostatic potential Φ, where

$$f_{\text{elec}} = \frac{1}{2}\rho\Phi = \frac{q}{2}(c - c_0)\,\Phi. \tag{11}$$

The potential Φ must satisfy Poisson's equation,

$$\nabla \cdot [\epsilon \nabla \Phi] + \rho = 0, \tag{12}$$

where ϵ is the dielectric constant. We assume that c evolves much more slowly in time than Φ, that is, that the electrostatic potential adjusts instantaneously to the concentration field c. This a very reasonable assumption for the slow diffusive motion of the concentration field. Because of Eq. 12, ρ and Φ are not independent. To enforce the constraint of Eq. 12, we introduce a Lagrangian multiplier function $\lambda(\mathbf{r})$ and define a generalized free energy $\mathcal{L}$:

$$\mathcal{L} = F - \int_V \lambda(\mathbf{r}) \left[\nabla \cdot (\epsilon \nabla \Phi) + \rho \right] dV. \tag{13}$$

This allows us to consider c, Φ, and λ to be independent. From this point forward, the problem works with the generalized free energy $\mathcal{L}$. We require that $\mathcal{L}$ be stationary with respect to first variations of λ and Φ for a given charge distribution ρ. Physically, this will minimize the free energy F while at the same time ensure that Φ satisfies Poisson's equation. Taking the first variation of Eq. 13 with respect to λ, we obtain

$$\frac{\delta \mathcal{L}}{\delta \lambda} = 0 = \nabla \cdot (\epsilon \nabla \Phi) + \rho, \tag{14}$$

which simply (by construction) returns Poisson's equation. In addition, the first variation of Eq. 13 with respect to Φ gives

$$\frac{\delta \mathcal{L}}{\delta \Phi} = 0 = \frac{\rho}{2} - \nabla \cdot (\epsilon \nabla \lambda). \tag{15}$$

Comparing Eq. 15 with Eq. 12, we see that $\lambda = -\Phi/2$.

The time evolution equation of c is developed by considering the flow of particle currents, $\mathbf{j}_{\text{c}}$, and charge currents, $\mathbf{j}_{\text{q}}$, in the system. In general, when there are driving forces such as gradients in particle density and in electrostatic potentials, particles and charges will flow.

Because the particles carry charges these currents are related through the relation between c and ρ. The particle current $\mathbf{j}_\mathrm{c}$ is defined by

$$\mathbf{j}_\mathrm{c} = -M(c)\nabla\mu, \tag{16}$$

where $M(c)$ is the mobility (which can depend on the local concentration), μ is the chemical potential,

$$\mu = \frac{\delta\mathcal{L}}{\delta c} = -\kappa\nabla^2 c + \frac{\partial f}{\partial c} + \Phi\frac{\partial\rho}{\partial c} = -\kappa\nabla^2 c + \frac{\partial f}{\partial c} + q\Phi, \tag{17}$$

and $\mathbf{j}_\mathrm{c}$ obeys a continuity equation for mass conservation,

$$\frac{\partial c}{\partial t} = -\nabla\cdot\mathbf{j}_\mathrm{c} = \nabla\cdot(M\nabla\mu). \tag{18}$$

Equation 18 is the Cahn-Hilliard equation including electrostatics. Because the chemical potential μ in Eq. 17 now contains contributions from the electrostatic potential as well as from the chemical free energy density and the gradient energy density, it is usually referred to as the *electrochemical* potential. In addition, the charge density obeys the continuity equation,

$$\frac{\partial\rho}{\partial t} = -\nabla\cdot\mathbf{j}_\mathrm{q}. \tag{19}$$

Combining the continuity equation for ρ and the Cahn-Hillard equation,

$$\mathbf{j}_q = -q(M\nabla\mu) = q\mathbf{j}_c \tag{20}$$

results. In addition, $\mathbf{j}_q = -\sigma\nabla\mu$ for a normal linear medium, where σ is the conductivity. This relationship indicates that the conductivity and the mobility are related through $\sigma = qM$. The above indicates that the charge current arises both from a gradient in the charge density as well as from electric fields, i.e., $\mathbf{j}_q$ and $\mathbf{j}_c$ are directly related: for particles entering or leaving the system, a corresponding amount of charge also enters or leaves the system.

As stated previously, f_chem is taken as the same in the spinodal decomposition benchmark problem [1], i.e., a symmetric double-well function with minima between $0 < c < 1$,

$$f_\mathrm{chem} = w\left(c - c_\alpha\right)^2\left(c_\beta - c\right)^2, \tag{21}$$

where w controls the height of the double-well and c_α and c_β are the concentrations at which f_chem has minima. We choose a very simple concentration-dependent description,

$$M(c) = \frac{M_0}{1+c^2}, \tag{22}$$

for the concentration-dependent mobility.

The complete set of governing equations is given by Eqs. 23, 24, and 25, together with boundary conditions on c, μ, and Φ. Oftentimes, a split-operator formulation for the Cahn-Hilliard equation is more numerically tractable, thus Eqs. 23 and 24 are written separately,

$$\frac{\partial c}{\partial t} = \nabla\cdot\{M(c)\nabla\mu\} = -2M_0\frac{c}{(1+c^2)^2}\nabla c\cdot\nabla\mu + \frac{M_0}{(1+c^2)}\nabla^2\mu \tag{23}$$

$$\mu = 2w\left(c - c_\alpha\right)\left(c_\beta - c\right)\left(c_\alpha + c_\beta - 2c\right) - \kappa\nabla^2 c + q\Phi \tag{24}$$

$$\nabla^2\Phi = -\frac{q(c - c_0)}{\epsilon}. \tag{25}$$

The coupled Cahn-Hilliard-Poisson benchmark problem consists of solving two types of coupled Cahn-Hilliard-Poisson problems, parts (a) and (b), on two different computational domains, referred to as $D1$ and $D2$. Part (a) assumes that there is no external electric field and that the total mass (the integral of c over the domain) and total charge are conserved. Part (b) assumes that there is an external electric field $\mathbf{E}_{\text{ext}}$ applied and that mass may move in or out of the computational domain. The external field arises from different potentials applied to the left and right boundaries of the domains. Below, the common features to part (a) and part (b) are first described, then separate features for each problem are detailed.

Both part (a) and part (b) are defined by Eqs. 23, 24, and 25. The two different computational domains for both parts and are given to provide different levels of numerical complexity. The first domain, labeled $D1$, is a square 100×100 units in the xy-plane, with the bottom left corner at (0,0) and the top right corner at (100,100) (Fig. 2a). This domain geometry should be tractable for all numerical solution methods. The second domain, labeled $D2$, is a half-circle with a radius of 50 units attached to a rectangle that is 50 units wide in the $x-$direction and 100 units tall in the $y-$direction (Fig. 2b). This domain geometry is somewhat more challenging for numerical solvers. For all problems combinations, the initial condition for c is given by

$$\begin{aligned} c(x,y) &= c_0 + c_1 \left\{ \cos(0.2x)\cos(0.11y) + [\cos(0.13x)\cos(0.087y)]^2 \right. \\ &\quad \left. + \cos(0.025x - 0.015y)\cos(0.07x - 0.02y) \right\}, \end{aligned} \tag{26}$$

where $c_0 = 0.5$ and $c_1 = 0.04$. Note that this is the initial condition for the spinodal decomposition benchmark problem [1] with a slightly different parametrization. For all problem combinations, the other parameter values are $c_\alpha = 0.3$, $c_\beta = 0.7$, $\kappa = 2$, $w = 5$, $M_0 = 5$, $q = 0.3$, and $\epsilon = 10$.

As mentioned previously, part (a) does not include an external electric field and conserves the total mass and total charge within the domain. Natural boundary conditions $\mathbf{j_c} \propto \nabla\mu \cdot \hat{n} = 0$ ensure that there is no particle flux across the boundaries. Natural boundary conditions are also used for c and Φ. Because all of the boundary conditions are Neumann and there is no initial condition on Φ, the solution for Φ is not uniquely defined, i.e., the differential equations and the boundary conditions will be obeyed for any constant added to the solution. We uniquely specify the solution for Φ by setting $\Phi = 0$ at one point.

For part (a), the system of equations that has to be solved is defined by Eqs. 23, 24, and 25 together with the boundary conditions

$$\begin{aligned} \nabla\mu \cdot \hat{n} &= 0 \\ \nabla c \cdot \hat{n} &= 0 \\ \nabla\Phi \cdot \hat{n} &= 0, \\ \Phi(50,50) &= 0 \quad \text{on } D1, \\ \Phi(0,0) &= 0 \quad \text{on } D2, \end{aligned} \tag{27}$$

where $\hat{n}$ is an outward-pointing surface normal.

Unlike part (a), there is an external electric field $\mathbf{E}_{\text{ext}}$ applied for part (b). This field arises from different potentials applied to the left and right boundaries of the domains, i.e., Dirichlet boundary conditions are applied on Φ in this part. For simplicity, the left

and right boundaries are taken to be equipotential surfaces. In addition, the left and right boundaries are open for particle flux and the particle flux entering on one side is the same as the particle flux flowing out on the other side, so that total mass and charge inside the system are conserved,

$$\int_{\text{left}} M(c)\nabla\mu\cdot\hat{n}\,dS = -\int_{\text{right}} M(c)\nabla\mu\cdot\hat{n}\,dS, \tag{28}$$

where the surface integrals are over the left and right boundaries, respectively.

For computational domain D1, $\hat{n} = -\hat{x}$ and $\hat{n} = \hat{x}$ on the boundaries $y = 0$ and $y = 100$, respectively. The boundary conditions for D1 are

$$\begin{aligned} M(c)\nabla\mu\cdot\hat{n} &= +0.01,\ y = 0 \\ M(c)\nabla\mu\cdot\hat{n} &= -0.01,\ y = 100. \end{aligned} \tag{29}$$

This will ensure that the integrated incoming flux on the boundary $y = 0$ equals the outgoing flux on the boundary $y = 100$.

For computational domain D2, the surface normal on the left boundary $y = 0$ is $\hat{n} = -\hat{x}$. On the curved right boundary of D2, the surface normal can be taken as

$$\hat{n} = \cos\varphi\hat{x} + \sin\varphi\hat{y}, \tag{30}$$

where $\cos\varphi = (x-50)/\sqrt{(x-50)^2+(y-50)^2}$ and $\sin\varphi = (y-50)/\sqrt{(x-50)^2+(y-50)^2}$. On this domain, we take the boundary conditions to be

$$\begin{aligned} M(c)\nabla\mu\cdot\hat{n} &= +0.01,\ y = 0 \\ M(c)\nabla\mu\cdot\hat{n} &= -0.01\cos\varphi,\ \text{right boundary}. \end{aligned} \tag{31}$$

The boundary conditions for Φ are Dirichlet boundary conditions $\Phi = 0$ on the left and $\Phi = -\Phi_0$ on the right boundaries and Neumann boundary conditions on the top and bottom boundaries. Natural boundary conditions are applied for c, $\nabla c\cdot\hat{n} = 0$, on the top and bottom boundaries and the Dirichlet boundary condition $c = 0.5$ is applied on the left and right boundaries (see the Appendix for remarks on the boundary conditions).

In summary, part (b) is defined by Eqs. 23, 24, and 25 together with the boundary conditions on $D1$

$$\begin{aligned} M(c)\nabla\mu\cdot\hat{n} &= +0.01,\ \text{left side} \\ M(c)\nabla\mu\cdot\hat{n} &= -0.01,\ \text{right side} \\ \nabla c\cdot\hat{n} &= 0,\ \text{top and bottom} \\ c &= 0.5,\ \text{left and right sides} \\ \nabla\Phi\cdot\hat{n} &= 0,\ \text{top and bottom} \\ \Phi &= 0,\ \text{left side} \\ \Phi &= -\Phi_0,\ \text{right side}, \end{aligned} \tag{32}$$

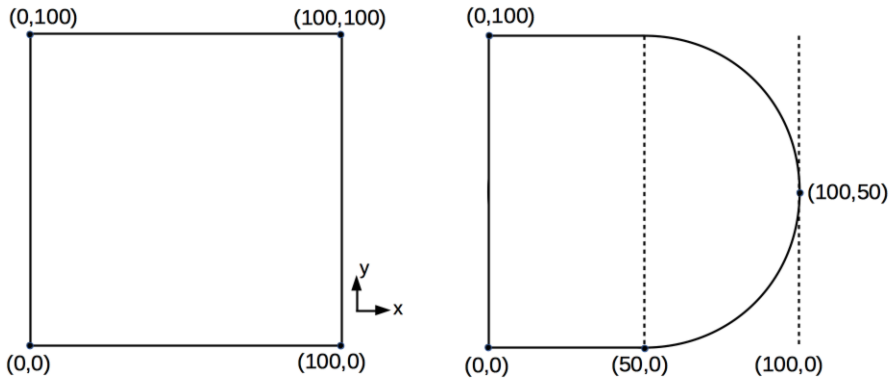

(a) (b)

Figure 2: Schematic illustration of the 2D computational domains (a) $D1$ and (b) $D2$ for the coupled Cahn-Hilliard-Poisson benchmark problem.

and on $D2$

$$\begin{aligned} M(c)\nabla\mu\cdot\hat{n} &= +0.01, \text{ left side} \\ M(c)\nabla\mu\cdot\hat{n} &= -0.01\cos\varphi, \text{ right side} \\ \nabla c\cdot\hat{n} &= 0, \text{ top and bottom} \\ c &= 0.5, \text{ left and right sides} \\ \nabla\Phi\cdot\hat{n} &= 0, \text{ top and bottom} \\ \Phi &= 0, \text{ left side} \\ \Phi &= -\Phi_0, \text{ right side.} \end{aligned} \tag{33}$$

For both domains, $\Phi_0 = 0.5$. We note that in our implementation of these problems in MOOSE, the values of c_0 are 0.509685652 for the square domain $D1$ and 0.510215727 for the curved domain $D2$.

All combinations of the coupled Cahn-Hilliard-Poisson benchmark problem involve finding the distributions of c and Φ as the system evolves to $t = 400$. In addition, the concentration field c and the potential field Φ are visualized and line cuts of c and Φ along the vertical line $y = 50$ are plotted at times $t = 5$, 10, 20, 50, 100, 200, and 400. The last metric is the plot the generalized free energy $\mathcal{L}$ of the system as a function of time.

3. Numerical methods

Example solutions to this set of benchmark problems are provided via an application based on the MOOSE computational framework [10, 11], as has been done in our previous two sets of benchmark problems [1, 2]. MOOSE is a flexible open-source finite element solver framework and includes phase field and fluid dynamics modules. We use MOOSE in this work to provide one set of solution data on the benchmark website as a basis for comparison with the results of other numerical solution methods and implementations.

3.1. Numerical methods applied to the Stokes problem

The details for the Stokes simulations are given below. Four sets of simulations are performed to illustrate errors that arise from poor mesh resolution. One set of simulations uses a high mesh resolution, which serves as the reference solutions. Three other sets of simulations are run with decreasing mesh resolution, denoted as "fine," "mid," and "coarse". Simulations are performed for both Stokes problems (with and without the obstruction). Second-order Lagrange shape functions are employed for u_x and u_y, and first-order Lagrange shape functions are employed for p. The finite element mesh for the first problem is created with the internal MOOSE mesh generator and second order quadrilateral elements are used. The coarse, mid, fine, and reference meshes contain one, 60×12, 120×24, and 300×60 elements, respectively. This translates to an element size of 30×6 units for the coarsest mesh, and elements of sizes 0.5, 0.25, and 0.1 units, respectively, for the mid, fine, and reference meshes. The finite element mesh for the second Stokes problem is created with gmsh [12], and the second-order triangles element are used because of the presence of the obstruction to allow for better meshing of the curved interface. Due to the non-uniform tiling of the elements, a characteristic length controlling the element size is defined, with the characteristic lengths being 1.0, 0.5, 0.25, and 0.1 units for the coarse, mid, fine, and reference meshes, respectively. For all of the Stokes simulations, single-matrix preconditioning with the block Jacobi preconditioner and incomplete LU factorization for sub-preconditioning is used, and a full Newton solve is performed. A nonlinear relative tolerance of 1×10^{-9}, a linear relative tolerance of 1×10^{-6}, a maximum of six nonlinear iterations per solve, and a maximum of 300 linear iterations, are specified.

3.2. Numerical methods for the coupled Cahn-Hilliard-Poisson problem

Below, details are given of the numerical parameters used to generate example solutions for the coupled Cahn-Hilliard-Poisson problem. As in the previous two benchmark papers, [1, 2], the Cahn-Hilliard equation is split into two second-order equations [13, 14] to avoid computationally expensive fourth-order derivative operators. The finite element mesh for the square computational domain is created with the internal MOOSE mesh generator, while the mesh for the half-curved domain is created with gmsh [12]. For the square domain, square first order quadrilateral elements with a side length of 0.5 units are used. For the half-curved domain, elements are first-order triangles with a characteristic length of 0.5 units.

Time integration is performed with the second-order backward differentiation (BDF2) time integrator in MOOSE and the "IterationAdaptiveDT" time stepper, which attempts to maintain a constant number of nonlinear iterations. The initial $dt = 0.1$ and the time step is allowed to grow by 5%, with the algorithm targeting five nonlinear iterations per time step with an iteration window of ± 1. For all these simulations, single-matrix preconditioning with the additive Schwarz preconditioner is applied with ILU sub-preconditioning for the full Newton solve. A nonlinear absolute tolerance of 10^{-11} and a maximum of 100 linear iterations are selected; MOOSE defaults are otherwise used. We set tolerances to be 10^{-11} for the relative tolerance, and 10^{-12} for the absolute tolerance.

4. Results and discussion

In this section, we discuss the example solutions and metrics obtained from them. For the Stokes problem, we also study error and convergence behavior based on the L_2 norm and local errors. Furthermore, we discuss some peculiar issues that may arise in solving these benchmark problems, especially the Stokes problem. We also describe certain subtleties in the coupled Cahn-Hilliard-Poisson problem and simple checks on the electrostatic potential and the total mass, as mass may be non-conserved when the system is over-determined with Neumann boundary conditions on c. Our input files, data and code are available in the Materials Data Facility [15] (https://materialsdatafacility.org) through DOI [to be supplied at time of publication].

4.1. Stokes problem

The Stokes problem, especially part (a) without the obstruction, is a simple problem in the area of fluid systems. Nevertheless, it was found during the course of the benchmark problem development that many of the public-domain codes for phase field simulations needed some significant modifications to handle the mathematical formulation, as it is a steady-state problem rather than a transient problem. While the actual solution is rather trivial, the difficulty lies in finding or implementing a Stokes solver, and the simplicity of part (a) aids in establishing a working, accurate solver. In addition, while not specifically related to the Stokes mathematics, we found that the presence of the internal obstruction uncovered an area to improve adaptive meshing in the MOOSE framework.

We first discuss the general nature of the solutions without and with the obstruction. The pressure and velocity components (v_x, v_y) for the Stokes problem with and without an obstruction are shown in Fig. 3 for the "reference" solution in each case, that is, the highest resolution for which the problems are solved. The pressure field in the unobstructed channel (Fig. 3a) changes smoothly over the entire domain with a relatively large change in the y-direction due to gravity and very slight changes in the x-direction. (Without the effect of gravity, the pressure will decrease from left to right with a uniform vertical profile.) In contrast, the obstruction disrupts the flow and leads to more complicated pressure (Fig. 3b) and velocity (Fig. 3d and 3f) profiles. The pressure is generally higher in the channel with the obstruction than without it, due to the need for more forcing (pressure) to satisfy the imposed boundary conditions when a flow obstruction is present. The pressure is higher to the left of the obstruction and drops rapidly as the fluid flows through the narrow portions between the obstruction and the walls. To the right of the obstruction, the pressure drops smoothly as it did in the simulation without the obstruction.

Similar comparisons are made with the velocity components. Without the obstruction, the velocity field is simple and keeps the profile set at the inlet boundary (Figs. 3c and 3e). However, the velocity is much different with the obstruction. In the vicinity of the obstruction, v_y is non-zero as the fluid has to flow in the $\pm y$-direction to avoid the obstruction, and v_x is highest directly above the obstruction (the wider channel around the obstruction). To the right of the obstruction, after a distance of about twice the width of the obstruction, the velocity retains the same profile as the simulation without the obstruction. Line cuts of the p, v_x, and v_y profiles for the simulations with and without the obstruction are shown in Fig. 4 for the lines $y = 5$ and $x = 7$. The pressure drops linearly (Fig. 4a) as a function of y

because of the presence of the gravitational field, while Fig. 4c shows the increase in pressure above the obstruction and subsequent drop to its level without the obstruction as we move along the channel away from the obstruction. Without the obstruction, the v_x component maintain its parabolic shape as function of y imposed by the inflow boundary condition with almost no discernible in v_y (Fig. 4b). In contrast, v_x has large maxima above and below the obstruction as the fluid has to speed up in the narrow channels in order to maintain laminar divergenceless flow. Figure 4d shows the maximum in v_x above the obstruction as well as the acquired v_y component in the vicinity of the obstruction.

We then examine numerical behavior via the computed L_2 error by performing a convergence study to understand how the L_2 error varies with mesh resolution. The global L_2 error is computed as $\sqrt{\int (\eta - \eta_{\text{ref}})^2 \, dV}$, while the local error is calculated as $\eta_{\text{ref}} - \eta$, where η refers to the variable in question, and η_{ref} is a reference solution. The results are shown in Fig. 5. For the simulations without the obstruction, the L_2 errors for p, v_x, and v_y are extremely small. Interestingly, the error increases slightly for p and v_x with the higher number of degrees of freedom (DOFs), and we suspect this is simply due to accumulation of round-off error in the post-processor used to calculated the error. While these results are atypical for a convergence study, they are understandable because the solution is trivial and may be described with only one element for the entire computational domain. However, the L_2 error follows the expected behavior for the non-trivial problem with the obstruction: the error decreases as number of DOFs increases. In order to gain some insight into the error behavior, we examine the local error. The local error for p is shown in Fig. 6 for both the finest mesh tested with respect to the reference solution and the coarsest mesh. The error is greatest in the elements on the boundary around the highest-curvature regions of the obstruction, but becomes negligible to the right of and away from the obstruction as the solution becomes very smooth. The error behavior for v_x and v_y is similar (not shown). These results indicate that the mesh should be modified to place the highest concentration of DOFs, that is, use the smallest elements near the high-curvature regions of the obstruction where the flow is non-trivial, while lower resolution is acceptable at regions far from the obstruction.

Finally, in the course of developing the benchmark problem, we discovered an unanticipated behavior with respect to adaptive meshing while using the MOOSE framework. We found that adaptive meshing did not correctly snap the nodes to the curved interior surface, essentially moving and distorting that curved internal surface. This was communicated to MOOSE developers and a the code was soon updated to provide the correct behavior. This is an example of the unanticipated utility of benchmark problems and the strength of collaborative, open-source software development.

4.2. Coupled Cahn-Hilliard-Poisson problem

The coupled Cahn-Hilliard-Poisson problem is an extension of the spinodal decomposition benchmark problem [1]; the parameters in the new problem are selected to generate a clear and discernible effect by the electrostatic field on the spinodal decomposition. In the absence of an applied electric field, the evolution of the coupled system is driven to minimize its total energy by balancing competing forces, i.e., the bulk and interfacial energies drive the system toward homogeneous domains with compositions of $c = c_\alpha$ and $c = c_\beta$ with a minimal

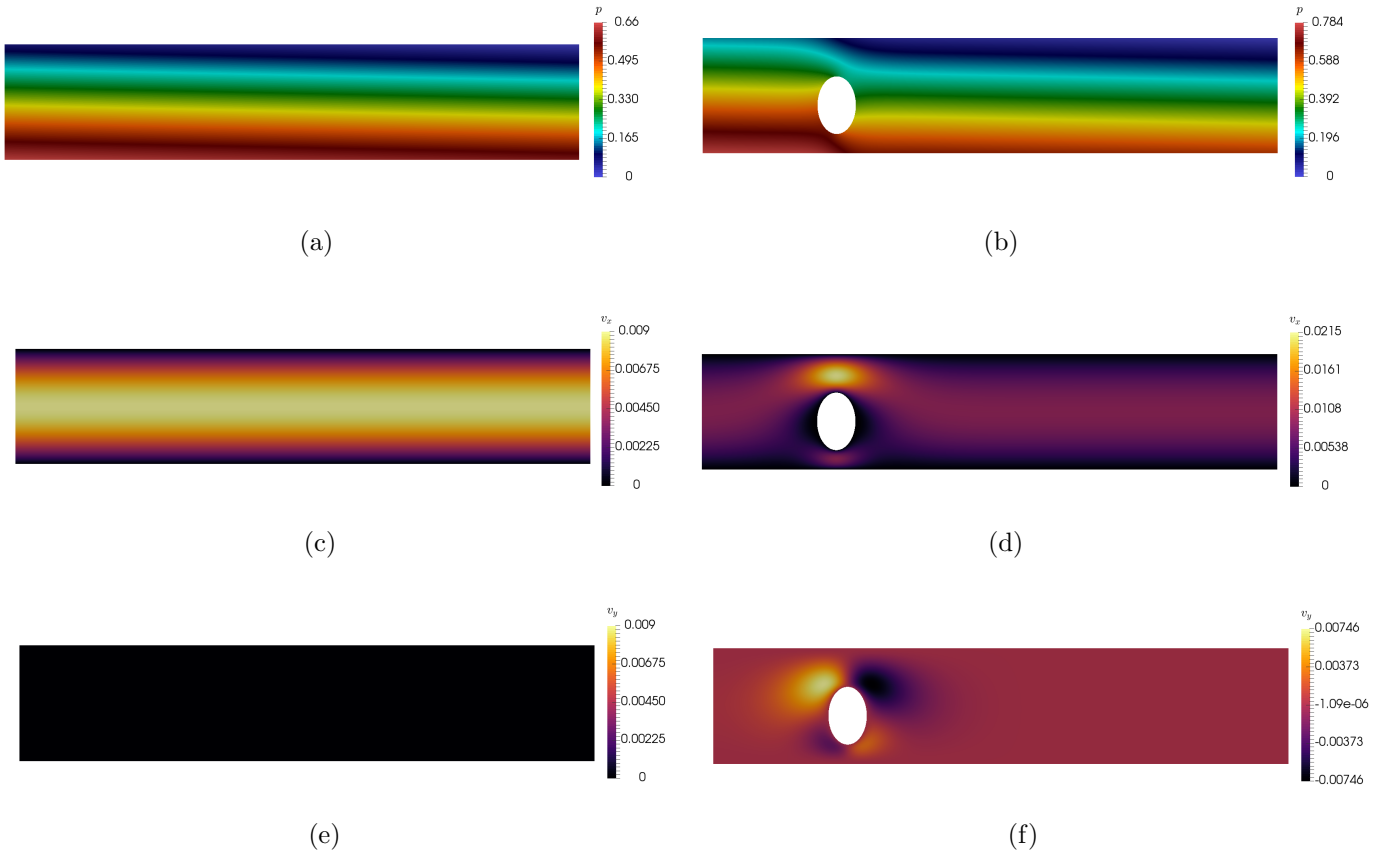

Figure 3: The pressure and velocity component fields for the Stokes benchmark problems a, c, e) without and b, d, f) with the obstruction. a, b) Pressure field; c, d) v_x field; e, f) v_y field. Data are shown for the reference solution.

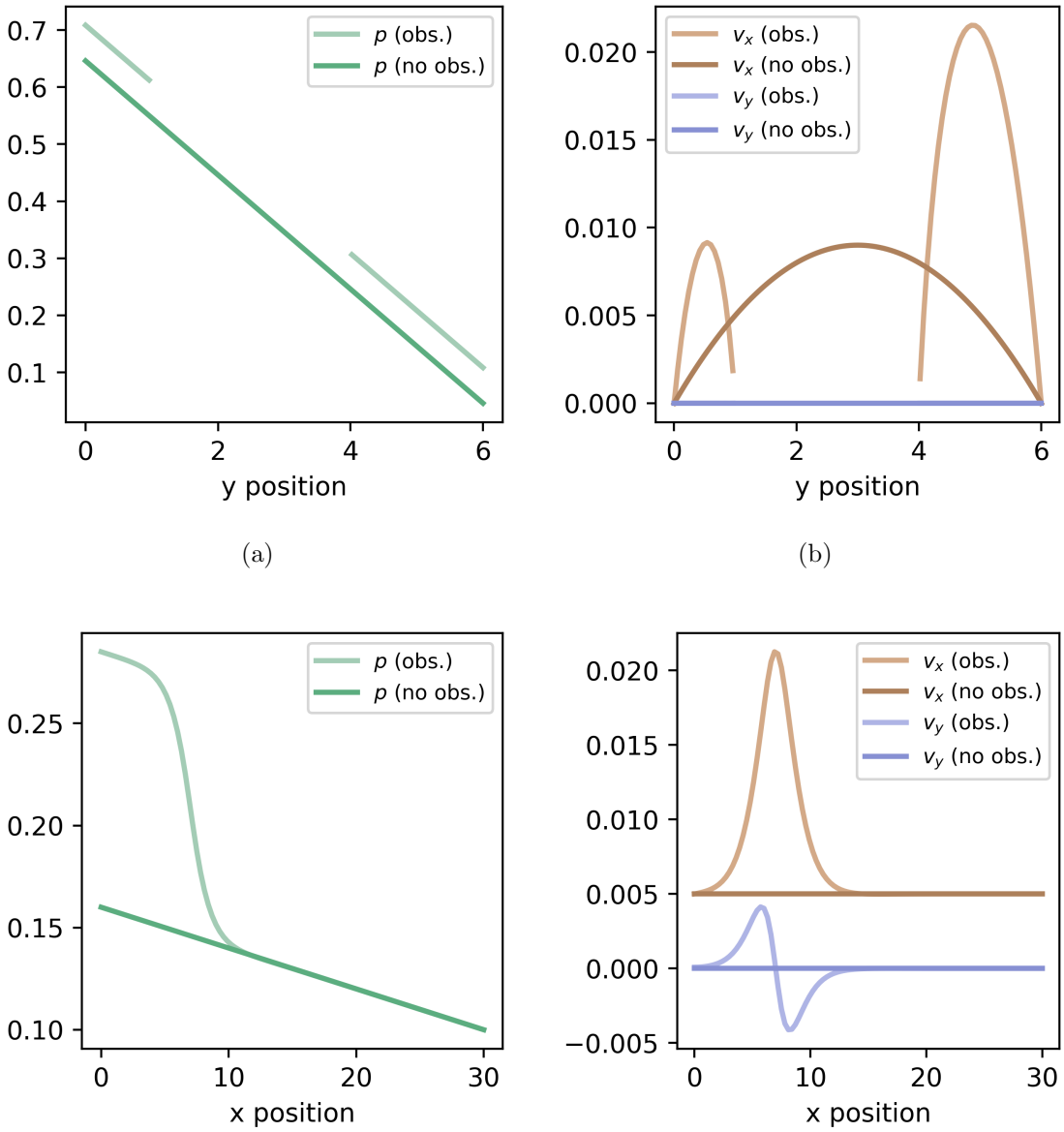

Figure 4: Line cuts through the computational domains for the Stokes benchmark problem with and without the obstruction. a) Pressure profile and b) velocity profiles for $x = 7$ (note the overlap in v_y profiles), c) pressure profile and d) velocity profiles for $y = 5$. Gaps in the lines indicate the presence of the obstruction. Data are shown for the reference solution.

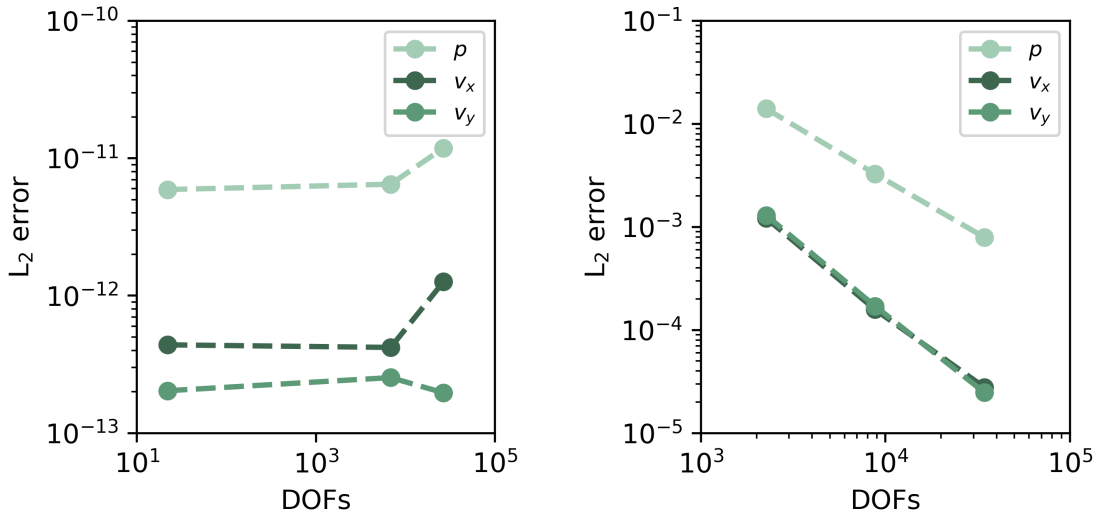

(a) (b)

Figure 5: Convergence plot of the global L_2 error versus degrees of freedom (DOFs) for the Stokes problem a) without the obstruction, b) with the obstruction (note the overlap in v_x and v_y). The solution for the problem without the obstruction may be found with a single element, resulting in the extremely small and practically constant global L_2 error versus DOFs, while the non-trivial problem with an obstruction follows the typical convergence behavior, *i.e.*, reduction in error with increasing mesh resolution.

(a)

(b)

Figure 6: Local L_2 error in the pressure field for the Stokes benchmark problem with the obstruction, shown for a) the finest mesh and b) the coarsest mesh tested with respect to the reference solution. The error is greatest around the highest-curvature region of the obstruction.

interface between them, while the electrostatic energy drives the system toward a uniform charge (and therefore mass) distribution. Thus, if the electrostatic energy is much larger than bulk and interfacial energies, the mass distribution will be homogeneous. Conversely, if the electrostatic energy is negligible, the system will undergo spinodal decomposition. It is instructive and simple to observe these two behaviors by setting the dielectric constant to something large (e.g., 100) to suppress the electrostatic energy, or to something small (e.g. 1) to make the electrostatic energy dominate. Further discussion and derivation is included in the Appendix.

In the presence of an applied field, the total energy may not necessarily decrease monotonically with time, but for the parameters, initial conditions, and boundary conditions chosen here, the energy $\mathcal{L}$ is monotonically non-increasing. For sufficiently long times, the system will reach a steady state ($\partial c/\partial t = 0$) that will, for not too large applied electric fields, resemble the mass distribution in the absence of an applied electric field in the interior of the computational domain. The reason for this is that mobile charges (or mass, as the mobile charge distribution is proportional to the concentration field c) will initially move to screen the external field. That means that the interior of the domain will subsequently evolve under chemical and electrostatic forces generated by the mass and charge distributions themselves rather than the applied external field.

The evolution of the concentration field c from $t = 0$ to $t = 400$ for the half-curved computational domain D2 in the presence of an applied field is shown in Fig. 7. Mass flows towards the right curved boundary in response to the applied field, after which the interior evolves under a total electric field modulated by the mass/charge distribution. This is further illustrated in Fig. 8, which shows the concentration fields and electrostatic potentials at $t = 400$ for the domains D1 and D2 without an applied field (Figs. 8a, 8e, 8b, 8f), and with an applied field (Figs. 8c, 8g, 8d, 8h). These figures clearly show that the interior mass distributions are quite similar with or without the applied field; the main difference is that mass moves to screen the applied field (Figs. 8c, 8g), resulting in mass accumulation on the right boundary and mass depletion on the left boundary. Similarly, because the electrostatic potential must obey Poisson's equation locally, there are clear similarities between the electrostatic potential in the interior without (Figs. 8b, 8f) and with (Figs. 8d, 8h) an applied field. However, near the boundaries the electrostatic potential changes in the presence of an applied field as a combination of the charge accumulation/depletion and the boundary conditions on the electrostatic potential.

Line cuts at $y = 50$ of c (Fig. 9) and Φ (Fig. 10) are shown at different times t for the curved domain D2. Figure 9 clearly shows the similarities of the concentration field in the bulk, as well as the differences near the boundaries as mass (charge) moves to screen the applied field in Fig. 9b. This screening effect is clearly visible in Fig. 10b. At small times, the electrostatic potential decreases approximately linearly, reflecting the fact that the potential is largely due to the constant applied field as the charge distribution initially is fairly uniform. As the system evolves, charge moves to screen the applied field, and the potential distribution in the interior develops modulations similar to the potential without an applied field (Fig. 10a).

Figure 11 shows the evolution of the total energy of the system without and applied field (black line), and with an applied field (blue line). The total energy without an applied field decreases monotonically, as expected. It does so also in the presence of the applied field –

in this case energy flows out of the system due to the applied field (see Appendix).

Finally, some simple checks on the coupled Cahn-Hilliard-Poisson problem are discussed. As aforementioned, it is instructive to set $\epsilon = 100$ and $\epsilon = 1$ to make sure that the system evolves towards a regular spinodal decomposition or a uniform mass distribution, respectively. Another useful check is to calculate $c - \epsilon\nabla^2\Phi/q$ and to plot the difference between it and c_0. The difference should be zero everywhere to within numerical error, and the regions with the largest errors indicate where numerical errors arise from meshing or numerical algorithms. The total mass should also be monitored; by construction, it should be conserved. Finally, it is instructive to change the boundary conditions for part (b) from the specified Dirichlet boundary conditions $c = 0.5$ to Neumann boundary conditions $\nabla c \cdot \hat{n} = 0$ on the left and right boundaries. The system is now ill-defined; what the resulting solution or lack thereof probably depends on the numerical implementation of the solver. In our case, using MOOSE, the system converged nicely at each time-step, but the total mass was continuously decreasing.

5. Conclusion

The benchmark problems presented in this work are an addition to our ongoing work to develop benchmark problems for phase field modeling [1, 2]. Here, we expand the portfolio of benchmark problems to include a problem on Stokes flow in a simple but non-trivial geometry and a problem coupling the Cahn-Hilliard equation to the electrostatic Poisson equation. The Stokes problem is strictly speaking not a phase field problem in the traditional sense. However, we felt it is a problem with increasing importance as the Stokes formulation of fluid flow is applicable to meso- and nanoscale systems. Such systems are becoming extremely important in the area of, e.g., water filtration and purification. Because the benchmark problems are now being adopted in classroom teaching we felt that it is of great value to bring attention to this class of problems to help educate future STEM researchers, who will undoubtedly deal with water purification. Also, as mentioned in the Introduction, we found in our workshop that the Stokes problem stressed codes in unexpected ways, and therefore has real value as a benchmark problem for code developers.

The coupled Cahn-Hilliard-Poisson problem sits more squarely in the realm of traditional phase field problems. As discussed in the Introduction, this problem is a very simplified, yet foundational problem in electrochemistry, which is also an increasingly important research area as it is the heart of multiple fields, such as energy storage, battery science and technology, and electrolysis. In the course of developing this benchmark, we found that correctly posing and solving the problem involved multiple unexpected subtleties, and it is our hope that the discussions of these are of instructional value to practitioners, teachers, and students.

The development of these benchmark problems, as the ones before them, have relied very heavily on comments and feedback from the community. It is a great experience to work in this way with an enthusiastic and engaged community. In order to make these benchmark problems as useful as possible, we urge the community to continue to provide feedback for existing and possible additional benchmark problems at `https://pages.nist.gov/pfhub/`.

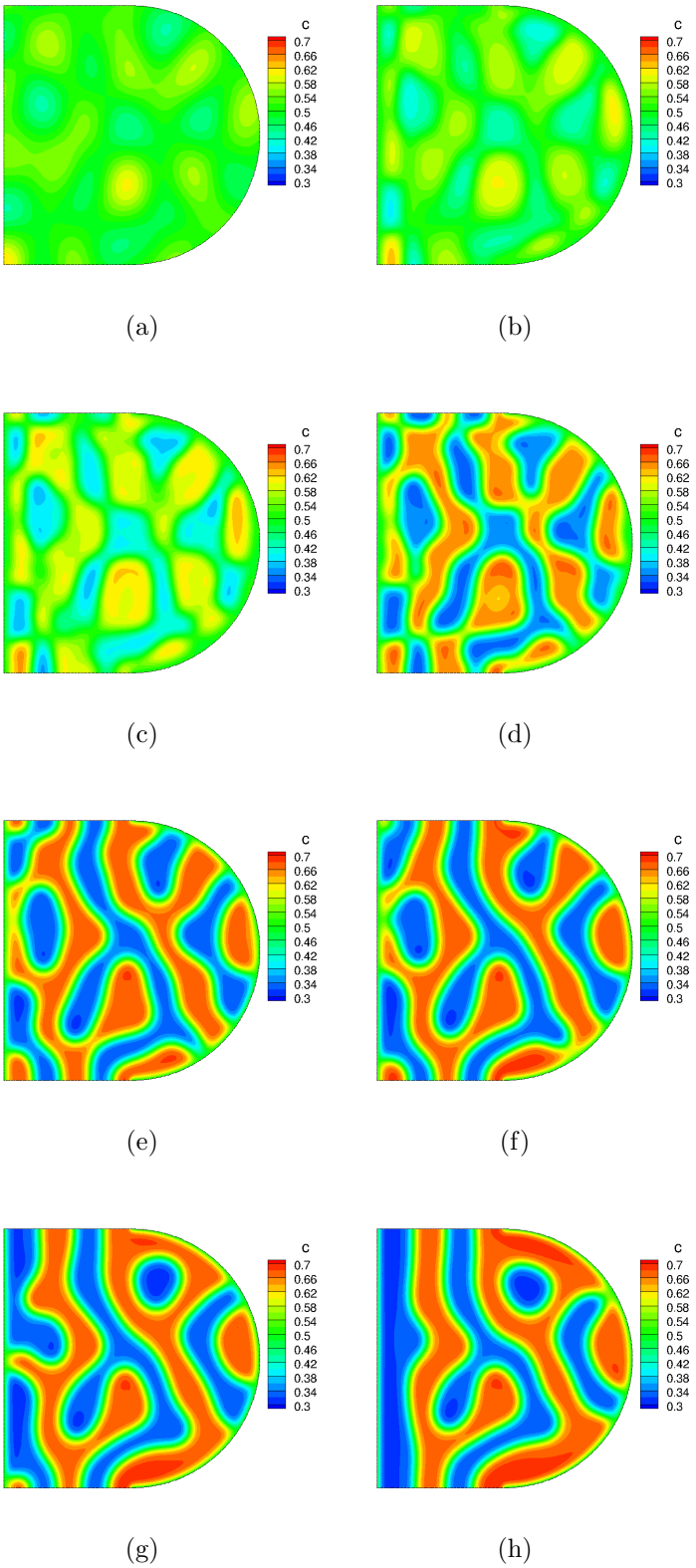

Figure 7: Composition field for the half-curved computational domain D2 in the coupled Cahn-Hilliard-Poisson benchmark problem with an applied external field. The evolution in the center of the domain proceeds initially as spinodal decomposition while the biased boundaries drive mass transport of the charged solute locally. The connected spinodal structure is broken as mass accumulates at right boundary and is depleted at the left one to screen out the external field as the system evolves. a) $t = 0$, b) $t = 5$, c) $t = 10$, d) $t = 20$, e) $t = 50$, f) $t = 100$, g) $t = 200$, h) $t = 400$.

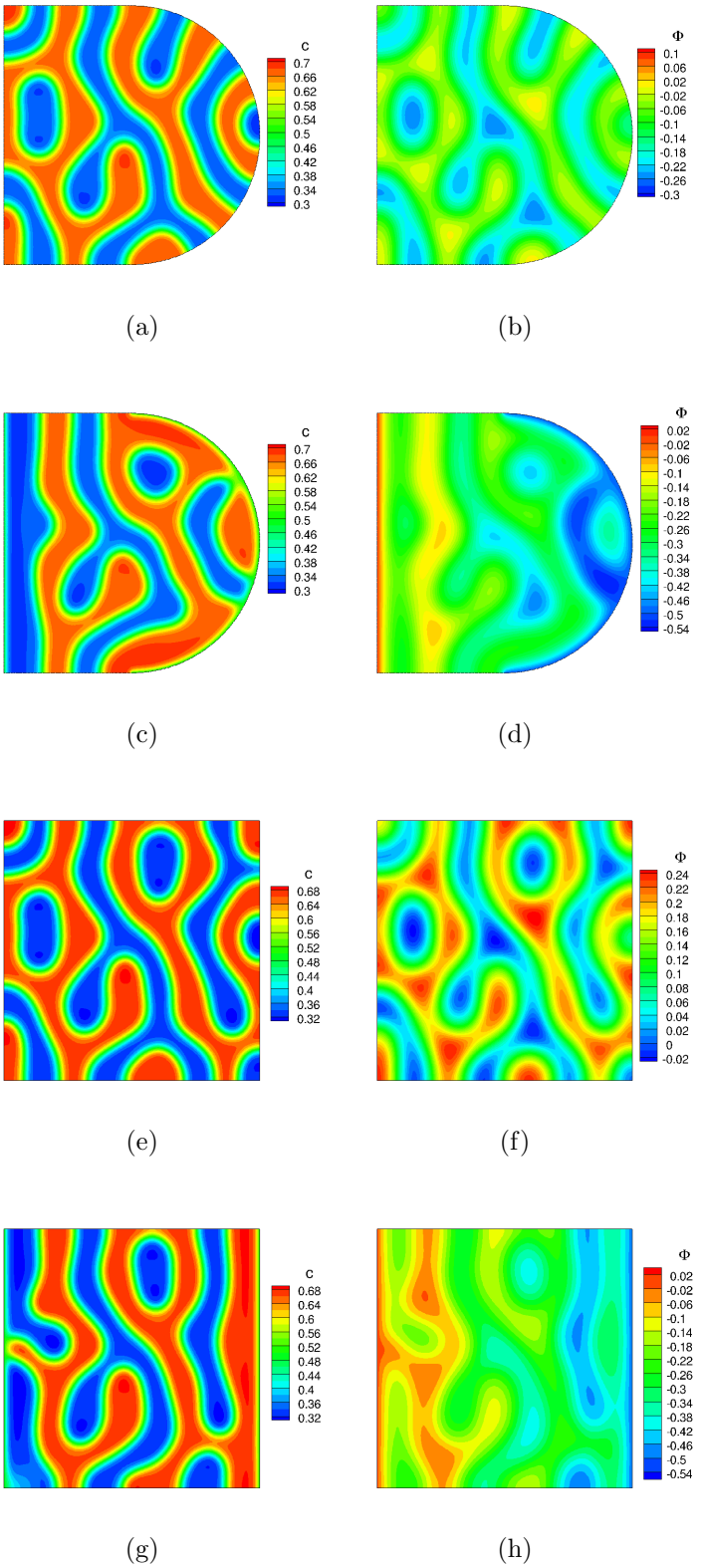

Figure 8: Additional examples of the c and Φ fields in the coupled Cahn-Hilliard-Poisson problem. The c and Φ fields at $t = 400$ for a, b) no external field, and c, d) with external field for the half-curved computational domain D2; with an applied field, Φ evolves as the composition field moves to screen out the external field. The results are similar for the square computational domain D1, as seen for the c and Φ fields at $t = 400$, e, f) no external field, and g, h) with an external field.

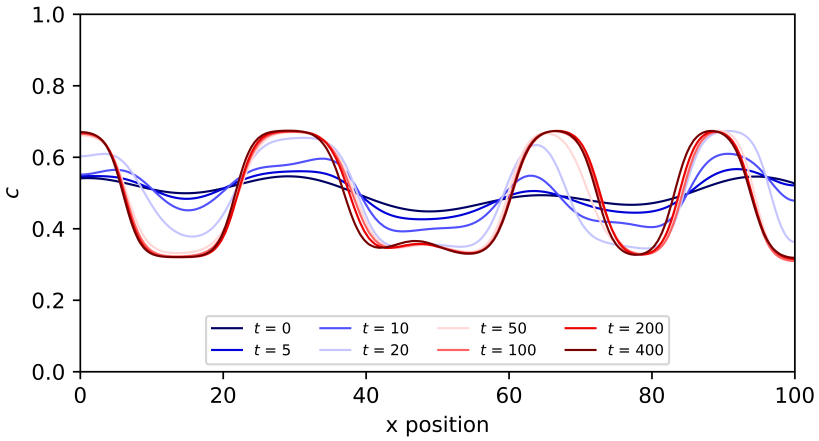

(a)

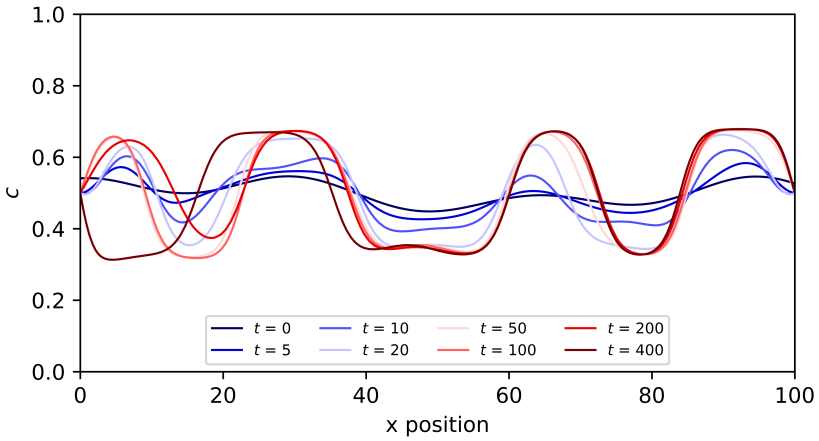

(b)

Figure 9: Line cuts of the c fields along $y = 50$ in the half-curved computational domain D2 for the coupled Cahn-Hilliard-Poisson benchmark problem a) without an external field, and b) in the presence of an external field. The evolution in the interior is similar, both without and with an external field. Near the boundary, mass/charge accumulates at the right and is depleted at the left boundary to screen out the external field.

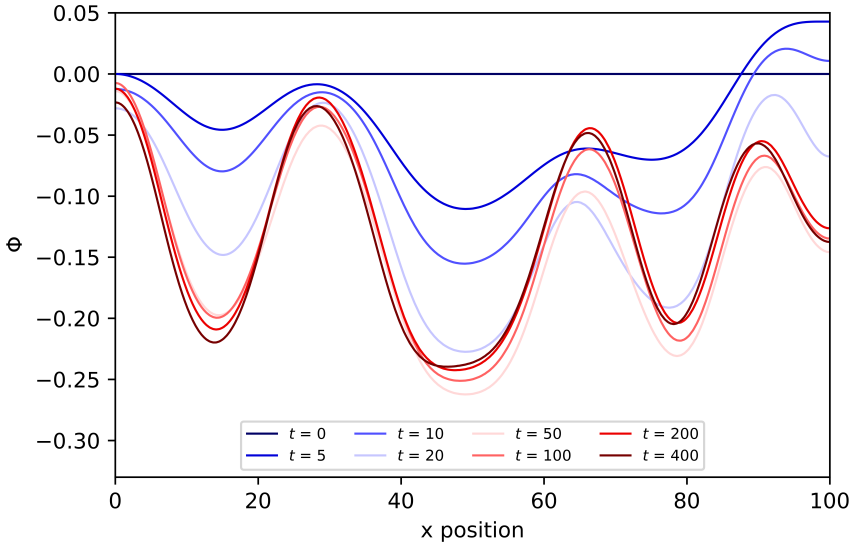

(a)

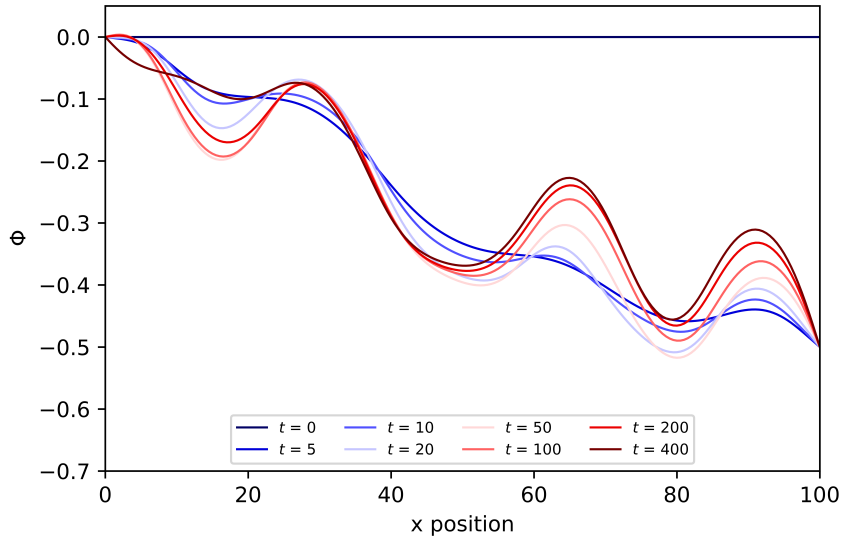

(b)

Figure 10: Line cuts of the Φ fields along $y = 50$ in the half-curved computational domain D2 for the coupled Cahn-Hilliard-Poisson benchmark problem a) without, and b) in the presence of an external field. Without an external field, the system evolves to minimize the total energy leading inhomogeneous mass and potential distributions. In the presence of an external field, mass/charge moves to screen out the external field, leading to modulated mass and potential distributions.

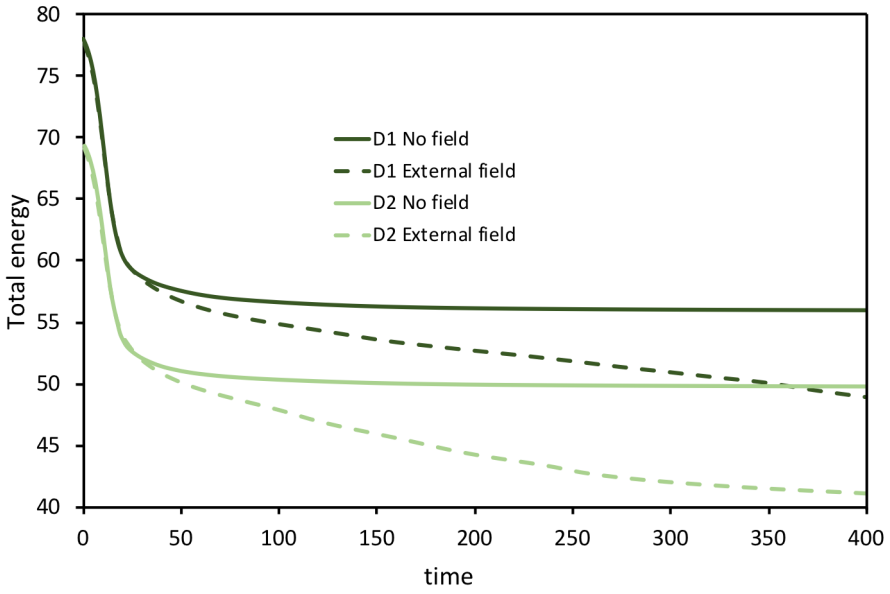

Figure 11: The total free energy (Eq. 10) for the square and half-curved computational domains in the coupled Cahn-Hilliard-Poisson benchmark problem. The higher energy for the square domain is due to the larger area. Note that in the presence of the external field, the total energy continues to decrease monotonically within the simulation time as energy is flowing out of the system.

Acknowledgments

This work was performed under financial assistance award 70NANB14H012 from U.S. Department of Commerce, National Institute of Standards and Technology as part of the Center for Hierarchical Material Design (CHiMaD). We gratefully acknowledge the computing resources provided on Bebop/Blues and Fission, high-performance computing clusters operated by the Laboratory Computing Resource Center at Argonne National Laboratory and the High Performance Computing Center at Idaho National Laboratory, respectively. We particularly thank the participants of the Phase Field Workshops held in Evanston, IL, to whom we are deeply indebted for invaluable feedback and comments.

Data Availability Statement

The raw data required to reproduce these findings are available to download from `http://dx.doi.org/XYZ`. The processed data required to reproduce these findings are available to download from `http://dx.doi.org/ZZZ`. [Addresses will be supplied at time of publication.]

Appendix

The Cahn-Hillard equation leads to a monotonically non-increasing total free energy F. The constrained generalized free energy $\mathcal{L}$ of the coupled Cahn-Hilliard-Poisson problem does the same. This can quickly be checked; as before, we use Lagrange mulipliers to enforce the constraint. For simplicity, let us first write

$$f(c, \nabla c, \Phi) = \frac{\kappa}{2}|\nabla c|^2 + f_{\text{chem}} + \frac{1}{2}\rho\Phi, \tag{34}$$

then,

$$\mathcal{L} = \int_V f(c, \nabla c, \Phi)\, dV - \int_V \lambda(x) \left[\nabla \cdot (\epsilon \nabla \Phi) + \rho\right]\, dV \tag{35}$$

and

$$\frac{d\mathcal{L}}{dt} = \int_V \left[\frac{\partial f}{\partial c}\frac{\partial c}{\partial t} + \frac{\partial f}{\partial \nabla c}\frac{\partial \nabla c}{\partial t} + \frac{\partial f}{\partial \Phi}\frac{\partial \Phi}{\partial t} - \lambda(\mathbf{r})\frac{d\rho}{dc}\frac{\partial c}{\partial t} - \frac{\partial \Phi}{\partial t}\nabla \cdot \epsilon \nabla \lambda(\mathbf{r})\right]\, dV. \tag{36}$$

The last term in Eq. 36 comes from integrating $\lambda(\mathbf{r})\nabla \cdot (\epsilon \nabla \Phi)$ twice by parts and noting that the terms that appear involving the volume integral of the divergence cancel. We can now eliminate $\lambda = -\Phi/2$, note that the third and fifth terms of Eq. 36 cancel, and integrate by parts to find that

$$\frac{d\mathcal{L}}{dt} = \int_V \left[\mu \frac{\partial c}{\partial t} + \nabla \cdot \left(\frac{\partial f}{\partial \nabla c}\frac{\partial c}{\partial t}\right)\right]\, dV. \tag{37}$$

We replace $\partial c/\partial t = -\nabla \cdot \mathbf{j}_\mathrm{p}$ and integrate by parts again:

$$\frac{d\mathcal{L}}{dt} = \int_V \left[\nabla \mu \cdot \mathbf{j}_\mathrm{p} - \nabla \cdot \left(\frac{\partial f}{\partial \nabla c}\nabla \cdot \mathbf{j}_\mathrm{p} + \mu \mathbf{j}_\mathrm{p}\right)\right]\, dV. \tag{38}$$

We can make things more transparent by using $\mathbf{j}_\mathrm{p} = -M(c)\nabla \mu$:

$$\begin{aligned} \frac{d\mathcal{L}}{dt} &= \int_V \left[-M(c)\nabla \mu \cdot \nabla \mu + \nabla \cdot \left(\frac{\partial f}{\partial \nabla c}\nabla \cdot [M(c)\nabla \mu] + \mu M(c)\nabla \mu\right)\right]\, dV, \\ &= -\int_V M(c)\left[\nabla \mu\right]^2 + \int_{\partial V}\left(\frac{\partial f}{\partial \nabla c}\nabla \cdot [M(c)\nabla \mu] + \mu M(c)\nabla \mu\right) \cdot \hat{n}\, dS \end{aligned} \tag{39}$$

which shows that the total free energy will decrease if the surface terms (which are energy fluxes) vanish. Note that this result is independent of any implicit or explicit spatial- or concentration-dependence of M. Also, in the presence of an external electric field, the total energy $\mathcal{L}$ may increase or decrease depending on the flow of energy into or out of the system.

We close with a remark on the boundary conditions for c in part (b) of the Cahn-Hilliard-Poisson problem. The Cahn-Hilliard equation for c is a nonlinear time-dependent partial differential equation that is fourth-order in space and which in general requires two boundary conditions together with an initial condition. In the split formulation we have one second-order (in space) partial differential equation, and one time-dependent differential equation of second-order in space. These coupled equations can also be solved with one initial condition on c and two boundary conditions [16]. In many applications, the system is closed, so the physical boundary condition is no flux at the boundaries, $M\nabla \mu \cdot \hat{n} = 0$. Often, this is supplemented with the natural boundary condition for c arising from the variational problem of minimizing the free energy of the system, $\kappa \nabla c \cdot \hat{n} = 0$. When the system is not closed, energy is not necessarily conserved, so a natural boundary condition for ∇c certainly does not arise from any variational problem of minimizing the free energy. There is now flux in and out of the system and the boundary conditions are obtained by balancing flux of mass, momentum, charge, and energy at the interfaces. This is a topic beyond the scope of the benchmark problems considered here, but for pedagogical purposes, we will illustrate how assigning boundary conditions without careful consideration can lead to inconsistencies.

We return to the governing equation for c and consider this equation for given μ and Φ, at time t,

$$\kappa\nabla^2 c - \frac{\partial f}{\partial c} - q\Phi + \mu = 0. \tag{40}$$

Together with Dirichlet boundary conditions $c = c_i$ on boundary i, this is a well-defined partial differential equation. We can take the gradient of Eq. 40 and take the scalar product with $\hat{n}$ to get

$$\kappa\hat{n}\cdot\nabla\left[\nabla^2 c - \frac{\partial f}{\partial c}\right] - q\hat{n}\cdot\nabla\Phi + \hat{n}\cdot\nabla\mu \;\; = \;\; 0 \tag{41}$$

Note that Eq. 41 is trivially true as it follows directly from Eq. 40. Now, suppose that instead of Dirichlet boundary conditions, we have natural (Neumann) boundary conditions on c, $\nabla c\cdot\hat{n} = 0$. Because $\nabla\partial f/(\partial c) = \partial^2 f/(\partial c^2)\nabla c$, we can use the Neumann boundary condition $\nabla c\cdot\hat{n} = 0$ to remove the term in $\partial f/(\partial c)$. If we also assume (for simplicity and in order to illustrate a point) that the boundaries are along coordinate axes in a Cartesian coordinate system, then Eq. 41 becomes

$$\kappa\hat{n}\cdot\nabla\left[\nabla^2 c\right] - q\hat{n}\cdot\nabla\Phi + \hat{n}\cdot\nabla\mu = \kappa\nabla^2\left[\nabla c\cdot\hat{n}\right] - q\hat{n}\cdot\nabla\Phi + \hat{n}\cdot\nabla\mu = -q\hat{n}\cdot\nabla\Phi + \hat{n}\cdot\nabla\mu = 0. \tag{42}$$

This obviously does *not* hold if there are fluxes such that $-q\hat{n}\cdot\nabla\Phi + \hat{n}\cdot\nabla\mu \neq 0$.

References

[1] A. Jokisaari, P. Voorhees, J. E. Guyer, J. Warren, O. Heinonen, Benchmark problems for numerical implementations of phase field models, Computational Materials Science 126 (2017) 139–151.

[2] A. Jokisaari, P. Voorhees, J. E. Guyer, J. Warren, O. Heinonen, Phase field benchmark problems for dendritic growth and linear elasticity, Computational Materials Science 149 (2018) 336.

[3] H.-J. Diepers, C. Beckermann, I. Steinbach, Simulation of convection and ripening in a binary alloy mush using the phase-field method, Acta Materialia 47 (1999) 3663–3678.

[4] S. Sakane, T. Takaki, M. Ohno, Y. Shibuta, Simulation method based on phase-field lattice Boltzmann model for long-distance sedimentation of single equiaxed dendrite, Computational Materials Science 164 (2019) 39–45.

[5] J. E. Guyer, W. J. Boettinger, J. A. Warren, G. B. McFadden, Phase field modeling of electrochemistry. I. Equilibrium, Physical Review E 69 (2004) 021603.

[6] J. E. Guyer, W. J. Boettinger, J. A. Warren, G. B. McFadden, Phase field modeling of electrochemistry. II. Kinetics, Physical Review E 69 (2004) 021604.

[7] J. Deng, G. J. Wagner, R. P. Muller, Phase field modeling of solid electrolyte interface formation in lithium ion batteries, Journal of the Electrochemical Society 160 (2013) A487–A496.

[8] Y. Shibuta, S. Unoura, T. Sato, H. Shibata, M. Kurata, T. Suzuki, A phase-field simulation of uranium dendrite growth on the cathode in the electrorefining process, Journal of Nuclear Materials 414 (2011) 114–119.

[9] T. Ohta, K. Kawasaki, Equilibrium morphology of block copolymer melts, Macromolecules 19 (1986) 2621–2632.

[10] D. Gaston, J. Peterson, C. Permann, D. Andrs, A. Slaughter, J. Miller, Continuous integration for concurrent computational framework and application development, Journal of Open Research Software 2 (2014).

[11] D. R. Gaston, C. J. Permann, J. W. Peterson, A. E. Slaughter, D. Andrš, Y. Wang, M. P. Short, D. M. Perez, M. R. Tonks, J. Ortensi, et al., Physics-based multiscale coupling for full core nuclear reactor simulation, Annals of Nuclear Energy 84 (2015) 45–54.

[12] C. Geuzaine, J.-F. Remacle, Gmsh: A 3-D finite element mesh generator with built-in pre-and post-processing facilities, International journal for numerical methods in engineering 79 (2009) 1309–1331.

[13] C. M. Elliott, D. A. French, F. A. Milner, A second order splitting method for the Cahn-Hilliard equation, Numerische Mathematik 54 (1989) 575–590.

[14] M. R. Tonks, D. Gaston, P. C. Millett, D. Andrs, P. Talbot, An object-oriented finite element framework for multiphysics phase field simulations, Computational Materials Science 51 (2012) 20–29.

[15] B. Blaiszik, K. Chard, J. Pruyne, R. Ananthakrishnan, S. Tuecke, I. Foster, The Materials Data Facility: Data services to advance materials science research, JOM 68 (2016) 2045–2052.

[16] C. M. Elliott, The Cahn-Hilliard model for the kinetics of phase separation, in: Mathematical models for phase change problems, Springer, 1989, pp. 35–73.